Missouri S&T Library and Learning Resources

Scholars' Mine

Masters Theses

Student Theses and Dissertations

2011

Hall-effect thruster surface properties investigation

David George Zidar

Follow this and additional works at: https://scholarsmine.mst.edu/masters_theses

 Part of the Aerospace Engineering Commons

Department:

Recommended Citation

Zidar, David George, "Hall-effect thruster surface properties investigation" (2011). *Masters Theses*. 5424.
https://scholarsmine.mst.edu/masters_theses/5424

This thesis is brought to you by Scholars' Mine, a service of the Missouri S&T Library and Learning Resources. This work is protected by U. S. Copyright Law. Unauthorized use including reproduction for redistribution requires the permission of the copyright holder. For more information, please contact scholarsmine@mst.edu.

HALL-EFFECT THRUSTER SURFACE PROPERTIES INVESTIGATION

by

DAVID GEORGE ZIDAR

A THESIS

Presented to the Faculty of the Graduate School of the

MISSOURI UNIVERSITY OF SCIENCE AND TECHNOLOGY

In Partial Fulfillment of the Requirements for the Degree

MASTER OF SCIENCE IN AEROSPACE ENGINEERING

2011

Approved by

J. L. Rovey, Advisor
D. W. Riggins
K. M. Isaac
G. Hilmas

© 2011
David George Zidar
All Rights Reserved

ABSTRACT

Surface properties of Hall-effect thruster channel walls play an important role in the performance and lifetime of the device. Physical models of near-wall effects are beginning to be incorporated into thruster simulations, and these models must account for evolution of channel surface properties due to thruster operation. Results from this study show differences in boron nitride channel surface properties from beginning-of-life and after 100's of hours of operation. Two worn thruster channels of different boron nitride grades are compared with their corresponding pristine and shadow-shielded samples. Pristine HP grade boron nitride surface roughness is 9000±700 Å, while the worn sample is 110,900±8900 Å at the exit plane. Pristine M26 grade boron nitride surface roughness is 18400±1400 Å, while the worn sample is 52300±4200 Å at the exit plane. Comparison of pristine and worn channel surfaces also show surface properties are dependent on axial position within the channel. For example, surface roughness increases by as much as a factor of 5.4 and surface atom fraction of carbon and metallic atoms decreases by a factor of 2.9 from anode to exit plane. Macroscopic striations at the exit plane are found to be related to the electron gyroradius and give rise to anisotropic surface roughness. Smoothing of ceramic grains at the microscopic level is also found.

ACKNOWLEDGMENTS

I wish to express my gratitude to my thesis adviser Dr. Joshua Rovey. Without his patience, insights and guidance this work would not have been possible. I must also acknowledge my appreciation to the members of my thesis committee, Dr. David Riggins, Dr. Greg Hilmas and Dr. K. M. Isaac. I would also like to express my thanks to my colleagues in the Aerospace Plasma Laboratory at Missouri S&T for their many insights and enlightening conversations.

The financial assistance provided by the Missouri Space Grant Consortium, and the Materials Research Center at the Missouri S&T is greatly appreciated. Special thanks must also be given to Dr. Jay Switzer, Dr. Eric Bohannan and Mrs. Clarissa Wisner for granting access to and assistance with surface profilometry and scanning electron microscopy equipment. The generous donation of Boron Nitride Ceramic specimens from St. Gobain Advanced Ceramics is greatly appreciated.

On a personal level, I must express my gratitude to my fiancée Ms. Tracey Bertram for her endless patience, encouragement and support, without which I could never have completed this project. I would also like to express my appreciation to my parents David and Joan Zidar and to Edward and Susan Bertram for their support and encouragement.

TABLE OF CONTENTS

LIST OF ILLUSTRATIONS

LIST OF TABLES

NOMENCLATURE

Symbol	Description
$\vec{B}$	Magnetic Field Vector, T
$\vec{E}$	Electric Field Vector, V/m
$\vec{F}$	Force Vector on a Charged Particle, N
n	Total Number of Height Measurements Taken
q	Elementary Charge, C
R_a	Roughness, Å
r_e	Electron Gyroradius, cm
T_e	Electron Temperature, eV
$\vec{v}$	Velocity of a Charged Particle, m/s
y_i	Height of Surface Irregularity at Location i, Å

1. INTRODUCTION

1.1. BASIC OPERATIONAL HALL THRUSTER PHYSICS

Hall-effect thrusters (HETs) are an electric spacecraft propulsion system in which thrust generation is due to acceleration of ionized propellant called plasma. Typically, an HET has an annular geometry in which an axial electric field is crossed with a radial magnetic field. A cathode emits electrons that drift in the $\vec{E} \times \vec{B}$ direction, forming an azimuthal Hall current. Neutral propellant atoms, typically xenon, are injected through the anode into an annular insulating channel. Collisions between neutral xenon atoms and electrons drifting in the Hall current produce xenon ions that are accelerated by the electric field, resulting in thrust generation.

1.2. HISTORICAL NOTE ON HALL-EFFECT THRUSTERS

The HET was initially described in a form recognizable today by Seikel and Reshotko, in the Bulletin of the American Physical Society in 1962, where it was referred to as a Hall current ion accelerator [1]. A preliminary discussion of the device physics, and its potential application as a spacecraft propulsion system for deep space, and interplanetary science missions was published by NASA late in 1962 [2, 3]. The seminal work detailing the device physics and exploring its potential operational performance was published in the July 1964 *AIAA Journal* by Cann and Marlotte [4, 5]. Following this initial research into HETs, adoption of the HET was abandoned by NASA as a spacecraft propulsion system in favor of ion thrusters [5].

While in the West, interest in HETs waned after the late 1960s, the USSR engaged in extensive research into HETs, culminating with the flight of the first HET in December of 1971 [6]. This ÉOL-1 electric propulsion system, flew aboard the *Meteor 18* satellite marking the beginning of the practical use of Hall-thrusters in spaceflight. In the USSR, HETs were and still are referred to as stationary plasma thrusters or SPTs.

HETs were extensively researched by the USSR, and were used successfully on more than thirty satellites without a single failure [5, 6].

The collapse of the USSR marked a resurgence in Western interest in HETs for long duration deep space missions. The viability of the HET as an effective propulsion system for such missions was validated by the European Space Agency's (ESA), *SMART-1* spacecraft [7]. Launched in September 2003 *SMART-1* performed a 14 month transfer maneuver and reached lunar orbit in March of 2005 through electric propulsion alone. This flight demonstrated the capability of Solar Electric Primary Propulsion (SEPP). Propulsion for *SMART-1* was provided by a SNECMA PPS-1350, a 1500 W HET. This propulsion system was able to affect a lunar transfer of the 370 kg *SMART-1* spacecraft, and make additional maneuvers and orbit changes, and ultimately deorbit into the lunar surface, while carrying only 82 kg of Xenon propellant [8].

Research on HETs in the US is currently being conducted by a number of US government labs, and universities. HETs are currently being manufactured domestically by Aerojet and Busek Co. The first domestically manufactured HET to fly was a Busek BHT-200, which was launched in December of 2006 from Wallops Flight Facility aboard the Department of Defense (DOD) TacSat-2 technology demonstrator [9]. HET usage and research in the US has been on the rise since the late 1990s, and NASA is once again giving serious consideration to HETs for long duration space missions [10, 11].

1.3. NEAR WALL EFFECTS IN HETS

Modeling of HET plasma physics has been the subject of ongoing research [12-15]. Accurate models of HET thrusters can improve understanding of HET performance and lifetime, and aid development of more advanced, higher efficiency, and longer life designs. Many current HET efforts are focused on developing and benchmarking models that integrate the important role of surface properties of the annular channel that contains the plasma discharge [16, 17]. Wall-effects play an important role in both the lifetime and overall performance of the thruster. Properties of the channel wall can affect secondary

electron emission (SEE), anomalous electron transport, and near-wall conductivity, thereby altering HET performance [6, 18-20].

Further, wall properties are an important factor in the sputter erosion processes that are known to limit thruster lifetime [21- 24]. Current HET models do not integrate a realistic wall microstructure, but instead rely on sputter yield or SEE coefficients derived from idealized material tests [13, 17, 25]. Our results show that the surface properties inside the HET can be very different from those of a pristine test sample. Better understanding of the properties of the HET channel surface is required to produce accurate models of the near-wall physics within the HET channel.

The roughness of HET channel walls has been shown to affect the equipotential contours of the plasma sheath near the channel wall reducing overall thruster performance [26]. Raitses, *et al.,* shows that wall materials having higher SEE reduce the electron temperature within the HET discharge channel, thereby reducing thruster performance [5, 20]. Other studies have also shown increased efficiency in thrusters with channels having lower SEE [27, 28]. Surface roughness is known to play a role in SEE, [19] although, at present, no studies have been conducted to quantify the extent to which surface roughness modifies SEE. Determining the influence of material surface properties on SEE in HETs is difficult due to the complexity of electron-wall interaction, which must include factors such as roughness, composition, non-Maxwellian electron distribution, and multiple electron scattering processes all of which influence SEE yield, and as such have some level of influence on HET performance [14].

1.4. OBJECTIVE

Properties of the HET channel wall affect erosion and subsequently the lifetime of the thruster. The erosion of the channel surface, particularly in the acceleration region near the thruster exit plane, is attributed to sputtering of the channel wall material as a result of ion impact [29]. The sputter yield (atoms removed per incident ion) of the ceramic surface of a typical HET channel wall has been found to be dependent upon the roughness of the ceramic surface [30; 31]. Further, operation of an HET with different

channel material is known to produce different erosion rates. For instance, Peterson, *et.al.*, operated a 3 kW HET at the same operating condition for 200 hours with different grades of ceramic boron nitride (BN) channel material and showed that the total amount of erosion is dependent on the BN grade [32].

The goal of this study is to quantify the differences in surface properties of HET channel materials that have and have not been exposed to HET operation. This includes surface roughness, microstructure, and chemical composition. For the first time, clear quantifiable differences between HET channel surface properties at beginning-of-life and after 100's of hours of operation are presented. This study provides data on the actual surface roughness and wall microstructure inside a used/worn HET, results that may be integrated into wall models to better refine assumptions and simulation results.

2. MATERIAL SAMPLES

2.1. SAMPLE ORGANIZATION

Two main types of BN materials are investigated in this study: pristine and worn samples. Pristine BN samples are provided directly from the manufacturer and are machined using common HET fabrication techniques. Worn BN samples are obtained from research-grade HETs that have been operated for many hours. Further, there are two types of worn BN samples: those exposed to the plasma discharge and those physically shielded or covered ("shadow shielded"). For instance, a sample cut from a HET channel has an internal side that faced the plasma and an external side that was shielded. Each sample analyzed and referenced in this paper is indexed in Table 2.1, with sample number, BN grade, type (listed as either pristine, exposed, or shielded), and any other relevant information. Throughout this paper all samples are referred to by sample number.

Table 2.1. Index of Sample Numbers, with Corresponding BN Grade, Type, and Relevant Notes

Sample No.	BN Grade	Condition	Notes
A1	A	Pristine	Provided by St. Gobain Advanced Ceramics
B1	M	Pristine	Provided by St. Gobain Advanced Ceramics
C1	M26	Pristine	Provided by St. Gobain Advanced Ceramics
C2	M26	Exposed	Outer annulus of high-power thruster, Exposure ~2000 hours
C3	M26	Exposed	Inner annulus of high-power thruster, Exposure ~2000 hours

Table 2.1. Index of Sample Numbers, with Corresponding BN Grade, Type, and Relevant Notes (Continued)

C4	M26	Shielded	Shielded part of outer annulus of high-power thruster
C5	M26	Shielded	Shielded part of inner annulus of high-power thruster
D1	HP	Pristine	Provided by St. Gobain Advanced Ceramics
D2	HP	Exposed	Outer annulus of low-power thruster, Exposure ~600 hours
D3	HP	Shielded	Shielded part of outer annulus of low-power thruster

2.2. SPECIMEN DETAILS

Pristine samples of BN grade A, HP, M, and M26 are investigated. Grade A is composed primarily of BN with a boric acid binder [33]. Grade HP is composed primarily of BN with a 4.5% calcium borate binder [34]. Grade M is composed of 40% BN and 60% by weight amorphous silicon dioxide [35]. Grade M26 is composed of 60% BN and 40% by weight amorphous silicon dioxide [35]. The manufacturer's specified chemical composition for grade M26 is listed in Table 4.3, the manufacturer's specified chemical composition for grades A and HP are not publicly available. The test surface of each pristine sample is faced off with a carbide mill tool. The pristine specimens of grades A and HP are discs 12 mm in diameter and 3 mm high. The pristine grades M and M26 specimens are blocks 12 mm square and 3 mm high.

Two worn HET channels are investigated. The channels are from different research-grade HETs. These HETs have each been operated at multiple voltage and power levels. However, we are still able to categorize the power level and voltage range of each thruster. The first worn channel is grade M26 BN and was used in a high-power (>1 kW) HET for approximately 2000 hours over voltages ranging from 200-600 V.

Analyses on both the inner and outer wall of this channel are performed at multiple axial locations. The second worn channel is grade HP BN and was used in a low-power (< 1 kW) HET for approximately 600 hours over voltages ranging from 200-600 V. Only the outer wall of this channel is analyzed at multiple axial locations. Both channels show visible signs of erosion (chamfering, grooves, striations), but neither is considered to be at end-of-life because sufficient erosion has not yet occurred to expose the magnetic pole pieces of the HET. Both channels have regions that were covered ("shadow shielded") and therefore not exposed to plasma. These covered regions received the same fabrication and machining processes as those exposed to the plasma.

3. MATERIAL SAMPLE CHARACTERIZATION METHODS

Each material sample is characterized using surface profilometry, scanning electron microscopy (SEM), and energy dispersive x-ray spectroscopy (EDS). Profilometry quantifies the surface roughness of the sample, while SEM provides a qualitative comparison of the microscopic topography of the samples. Energy dispersive x-ray spectroscopy (EDS) is used to quantify the atomic constituents on the surface of each sample.

3.1. SURFACE PROFILOMETRY

Surface profilometry determines surface roughness by measuring the height of finely spaced irregularities. Roughness should not be confused with surface waviness, which is defined as surface irregularities having greater spacing than that of surface roughness. For surfaces which have been machined, roughness is generally a result of the machining operations, whereas waviness is generally a result of workpiece vibration, warping, or deflection during the machining process [36]. Quantitatively, surface roughness is measured as the height of surface irregularities with respect to an average line. Roughness is expressed in units of length; in the case of this study, roughness is expressed in angstroms. In this investigation, roughness, termed R_a, is determined using the arithmetical average, as defined in Eqn. 1:

$$R_a = \frac{\sum_{i=1}^{n} y_i}{n} \tag{1}$$

For this investigation, surface profilometry is performed using a Sloan Dektak IIA surface measuring system. The Dektak IIA is capable of measuring surface features having heights ranging from less than 100 Å to 655,000 Å [37]. Calibration and verification of accurate roughness measurements are conducted both before and after the roughness studies performed using this instrument. In all cases the profilometer is found to be accurate within the specified ±5% for all standards measured, which covered the specified measurement range from 100 Å to 655,000 Å [37]. Scanning electron microscope images of the tracks made by the scanning stylus of the profilometer demonstrate that the profilometer stylus tip has a characteristic width of 10-15 μm. The geometry of the stylus tip is assumed to be approximately hemispherical. The characteristic width of the stylus tip constrains the size of the surface features which can be measured in the direction of travel of the stylus tip. Therefore, the profilometer can make vertical measurements of surface having characteristic heights in the range of 100's of Å, while the measurements of the horizontal lengths of these features are limited to the 10's of μm. This model profilometer is a single line profilometer, meaning the roughness can only be measured along a single line on the sample surface. To better ensure that the roughness measurements reflect the roughness of an entire sample surface, multiple scans are taken at multiple locations.

3.2. SCANNING ELECTRON MICROSCOPY

A scanning electron microscope (SEM) uses electrons to produce images of surface features as low as 10 nm in size. An SEM operates by using an electron column consisting of an electron gun and two or more electrostatic lenses in a vacuum. The electron gun provides a beam of electrons having energies in the range of 1-40 keV, and the beam is reduced in diameter by electrostatic lenses to generate sharper images at high magnification. The electron beam interacts with the sample and penetrates roughly a micrometer into the surface, where electrons from the beam are backscattered and secondary electrons are emitted. Detectors collect the backscattered and secondary

electrons, and these electron signals are used to generate the magnified image of the specimen [38].

Secondary electrons emitted by the sample material are necessary to image the sample. Non-conducting insulators generally have poor secondary electron emission characteristics, in which case a conductive coating is often applied to provide high resolution, high magnification images. The ceramic specimens considered in this study are insulators, and a conductive coating is applied to provide the best imaging possible. In this study, a thin layer of 60:40 gold-palladium alloy is applied to the samples. The samples are placed into a vacuum chamber where the gold-palladium is sputtered onto the sample surface in a thin coat approximately 10 nm thick. The gold-palladium alloy provides high secondary electron emission, while still providing a thin, continuous film with minimal agglomeration regions. This thin coating provides the necessary secondary electrons for high resolution images, without obscuring the images of the underlying microstructure.

A Hitachi S-4700 scanning electron microscope is used to image the surface of each sample. It is capable of producing images with magnification greater than 500,000 times, and can resolve structures up to 2 nm across. For this investigation, micrographs were taken of each sample at magnifications of 30, 100, 400, 1,000, 5,000, and 10,000 times.

3.3. ENERGY DISPERSIVE X-RAY SPECTROSCOPY

The SEM used in this investigation has energy dispersive x-ray spectroscopy (EDS) capability. EDS is a variant of x-ray fluorescence spectroscopy, and is used for chemical characterization and elemental analysis. EDS is performed by a SEM which has been installed with the necessary detection equipment. The electron column creates an electron beam focused on the sample surface. This focused electron beam results in the generation of an x-ray signal from the sample surface. The x-ray photons generated from the interaction of the focused electron beam and the sample surface pass through a beryllium window separating the specimen vacuum chamber and the Lithium-drifted

Silicon detector. Within the detector, the photons pass into a cooled, reverse-bias *p-i-n* (p-type, intrinsic, n-type) Si(Li) crystal. The Si(Li) crystal absorbs each x-ray photon, and in response ejects a photoelectron. The photoelectron gives up most of its energy to produce electron-hole pairs, which are swept away by the bias applied to the crystal, to form a charge pulse. The charge pulse is then converted into a voltage pulse, which is then amplified and shaped by a series of amplifiers, converters, and an analog-to-digital converter where the final digital signal is fed into a computer X-ray analyzer (CXA) [38]. A histogram of the emission spectrum from the sample is obtained and analyzed by the CXA to determine the percent by weight of elements present in the sample. For this study, EDS analysis was conducted using an EDAX energy dispersive x-ray unit attached to the Hitachi S4700 SEM. Data provided by EDS is the chemical composition of the sample regions by both atom fraction and percent by weight.

Sample material characterization results using the three techniques described above are presented in this section. Specifically, surface roughness data obtained with profilometry measurements, surface photographs using high-magnification SEM, and sample chemical composition analysis from EDS are presented.

4. RESULTS

Sample material characterization results using the three techniques described above are presented in this section. Specifically, surface roughness data obtained with profilometry measurements, surface micrographs using SEM, and sample chemical composition analysis from EDS are presented.

4.1. SURFACE ROUGHNESS

Roughness measurements of the pristine samples are conducted. Each sample is characterized by taking multiple scans with the profilometer. Three scans, 5 mm long, spaced 2 mm apart are acquired. The sample is then rotated 90° and three additional 5 mm scans spaced 2 mm apart are acquired. These measurements are performed on each sample and the results averaged. Table 4.1 shows the average roughness for each BN grade. Grade HP is the smoothest at 9000 Å, while grade A has the highest roughness at 19500 Å. Grades M and M26, which are also chemically the most similar of the four grades, have similar surface roughness, differing only by 2%.

Table 4.1. Roughness of Each Pristine BN Grade Sample

Sample	BN Grade	Average Roughness [Å]
A1	A	19500
B1	M	18800
C1	M26	18400
D1	HP	9000

Surface roughness measurements for the worn and shielded C samples are presented in Figure 4.1 and Figure 4.2. Roughness of the C samples is measured using axial and azimuthal scans corresponding with the geometry of the thruster. For all worn and shielded C samples, 3 mm scans are acquired in both the azimuthal and axial direction. Results are presented as a function of distance from the exitplane of the HET. At each axial location, 3 axial scans and 3 azimuthal scans are conducted and the averaged results are presented. Error bars associated with these measurements are ±8%. This is based on the profilometer manufacturer quoted accuracy of ±5%, verified by testing with calibrated standards, plus the 95% confidence interval based on the repeated measurements (±3%).

Figure 4.1 shows roughness for the C2 and C3 samples. As Figure 4.1 shows, axial roughness on the outer channel wall (sample C2) ranges from 3.0 to 5.2 μm and, with the exception of a peak at 35 mm, remains relatively constant at about 3.8 μm and then increases to 5.2 μm near the exit plane. Azimuthal roughness of sample C2 is typically 1.5 to 2 times lower than axial roughness, except for a significant increase to 5.7 μm at the exit plane where azimuthal and axial roughness are comparable. Between 10 and 45 mm, azimuthal roughness is relatively constant, varying between 1.5 and 2.7 μm. Axial scans of the inner channel wall (sample C3) reveal axial roughness values that are 1.5 to 2 times lower than those obtained on the outer channel wall (sample C2). Axial roughness of the inner channel wall is similar in magnitude (within 5%) to the azimuthal roughness of the outer channel wall. Results for axial roughness of the inner channel wall are only presented at axial locations greater than 15 mm because the channel has a machined chamfer close to the exitplane making 3 mm scans unreliable due to curvature of the sample. In other words, the curvature of the sample causes the surface height to extend outside the range of the profilometer. While shorter scans are possible, to be consistent with the other C sample measurements only 3 mm scans are presented. For this same reason azimuthal roughness for sample C3 (inner channel wall) is not reported.

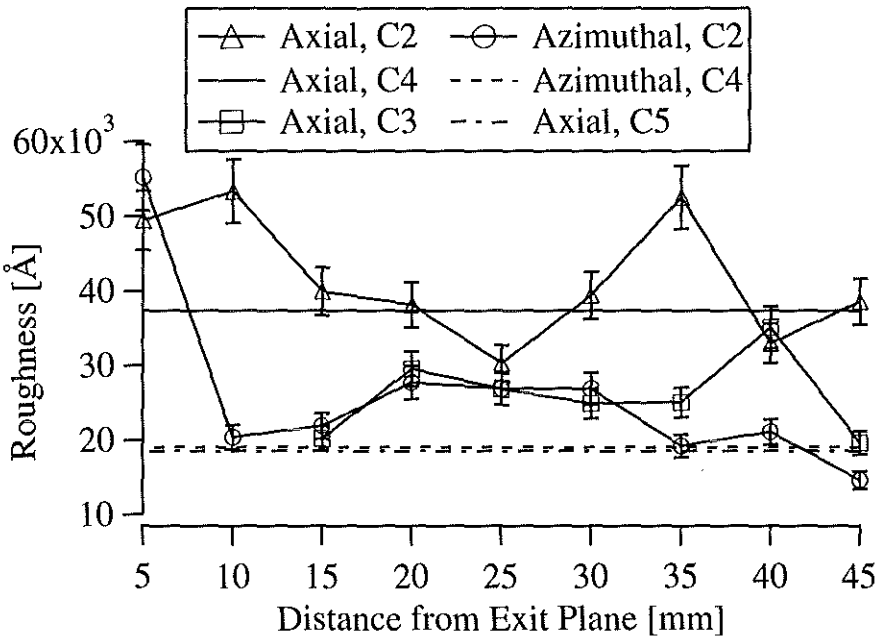

Figure 4.1. Sample C2, C3, C4, and C5 Roughness Measurements

Figure 4.1 shows roughness for the C4 and C5 samples. While 3 mm scans are still used for these samples, measurements are only acquired within the shielded region of the sample, which does not extend the full axial length of the sample. In other words, analysis of roughness variation with axial position for the shielded sample is not possible. Sample C4 (shadow shielded portion of outer channel wall) measurements show that the axial scan direction has roughness that is about 2 times larger than the azimuthal direction. This trend agrees well with that for sample C2, however, comparison of sample C2 and C4 axial and azimuthal roughness shows that C4 is generally smoother in both directions. Specifically, the shielded sample is 10% and 20% smoother in the axial and azimuthal directions, respectively. Comparison of sample C4 roughness with the pristine sample (C1) in Table 4.1 shows that the azimuthal direction of C4 closely matches the pristine value. However, the axial direction of C4 is 2 times rougher than the pristine sample. Sample C5 (shielded portion of inner channel wall) measurements show that the axial scan direction has roughness nearly identical to the C4 azimuthal scan. Further, C5

is about 30% smoother than its exposed counterpart, sample C3. Azimuthal 3 mm scans of C5 are not possible for the aforementioned channel curvature reasons.

Figure 4.2 shows composite roughness curves for C1, C2, and C4 samples. The composite roughness is the average of all roughness measurements in both the axial and azimuthal directions. Since only axial roughness is measured for samples C3 and C5, an average of azimuthal and axial roughness cannot be calculated. The shielded sample (C4) has roughness that is approximately 50% larger than the pristine sample investigated (C1). The roughest measured location on sample C2 is at 5 mm from the exitplane. From axial locations of 15 to 45 mm the roughness is relatively constant at approximately 3.1 μm and is on average only 10% greater than sample C4. However, at axial locations less than 15 mm, roughness increases to a maximum of 5.2 μm at 5 mm from the exitplane, an increase of 73%.

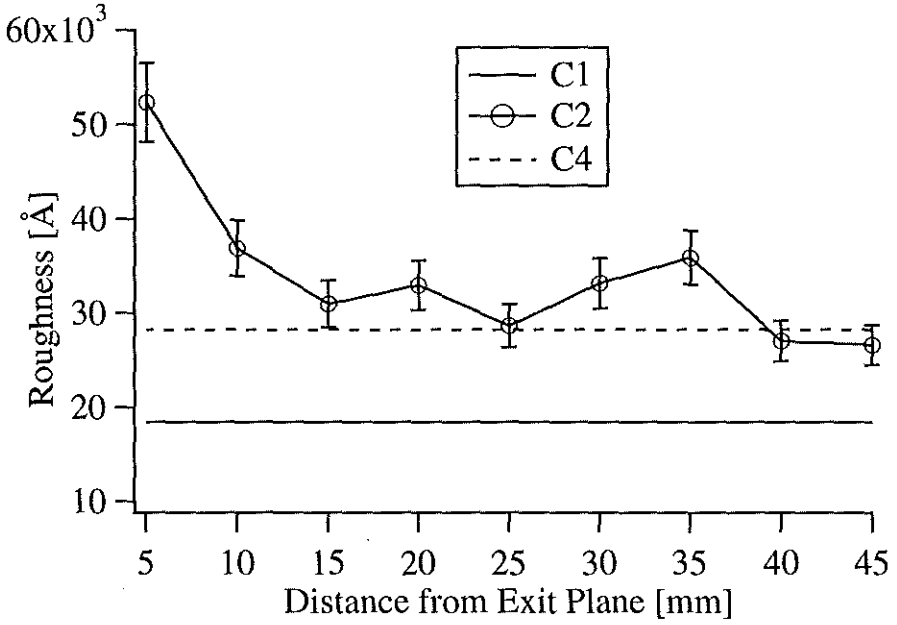

Figure 4.2. Average Roughness of All Measurements of Samples C1, C2, and C4

Sample D roughness measurements are shown in Table 4.2. Due to the smaller size and shorter channel of this HET (lower power generally equates to smaller size), profilometer scan lengths of only 1 mm are used at two main locations, near the anode and near the exitplane. With a shorter scan length both axial and azimuthal scans are completed. Error associated with these measurements is ±8% as described previously. Results show that the pristine sample (D1) has a roughness of about 0.9 μm, but the shielded sample (D3) has roughness of about 0.5 μm, almost half of the pristine sample. Both axial and azimuthal scans of D3 indicate approximately the same value of roughness, differing by only 5%, within the error of the measurements. The exposed sample (D2) has roughness significantly larger than D1 and D3. Further, the roughness of D2 is different in the axial and azimuthal directions, and at locations near the anode or near the exitplane. Near the anode the roughness is greatest in the azimuthal direction with a roughness values of 2.0 μm, while the axial direction has roughness of 1.3 μm. Near the exitplane the trend is reversed and the axial direction has greater roughness equal to approximately 13.2 μm with an azimuthal roughness of about 9.0 μm. Roughness near the exitplane is about 5.4 times greater than near the anode.

Table 4.2. Sample D Roughness Analysis

Region	Sample	Average Roughness [Å]	Scan	Condition
-	D1	9000	-	Pristine
Anode	D2	20000	Azimuthal	Exposed
Anode	D2	12800	Axial	Exposed
Exitplane	D2	89700	Azimuthal	Exposed
Exitplane	D2	132100	Axial	Exposed
-	D3	5600	Azimuthal	Shielded
-	D3	5300	Axial	Shielded

4.2. SCANNING ELECTRON MICROSCOPY

Scanning electron microscopy (SEM) imaging of the samples is performed at magnifications of 30, 100, 400, 1000, 5000, and 10,000 ×. Samples C1, C2, C4, D1, D2, and D3 are imaged. For the C samples, images with magnifications of 30, 1,000, and 10,000 × are presented in Figure 4.3, while magnifications of 30, 100, 1000, and 10,000 × are shown for D samples in Figure 4.4. For sample C2, SEM images are taken at the exit plane, 5 mm, 25 mm, and 45 mm from the exit plane. Sample C1 is the pristine sample, while C4 is the shielded sample. For sample D2, SEM images are taken near the exit plane and near the anode. Sample D1 is the pristine sample, while D3 is the shielded sample. In Figure 4.3 and Figure 4.4, in order to orient each photograph with respect to the thruster geometry, the arrow in each photograph points toward the exit plane of the HET channel. Qualitative description of SEM images of the C samples (Figure 4.3) is presented first, followed by D samples (Figure 4.4).

Figure 4.3 shows the surface features of the C samples. At low magnification (30x), the exit plane shows numerous deep scratches and grooves. Grooves in the azimuthal direction, as well as grooves angled at approximately 30° to the axial direction are visible (white circle in Figure 4.3). The angled grooves have a characteristic spacing of about 400 μm. Closer to the anode, at distances of 25 and 45 mm, scratches in the azimuthal direction are clearly visible. Visual comparison suggests that both the width and depth of grooves at the exitplane are larger than those at 25 or 45 mm. Further, the other locations do not show scratches or grooves in non-azimuthal directions. The scratched surface evident in the pristine image is due to the machining process applied to that sample. Similar markings are seen on the shielded, 25 mm, and 45 mm images and are also due to the HET channel machining process.

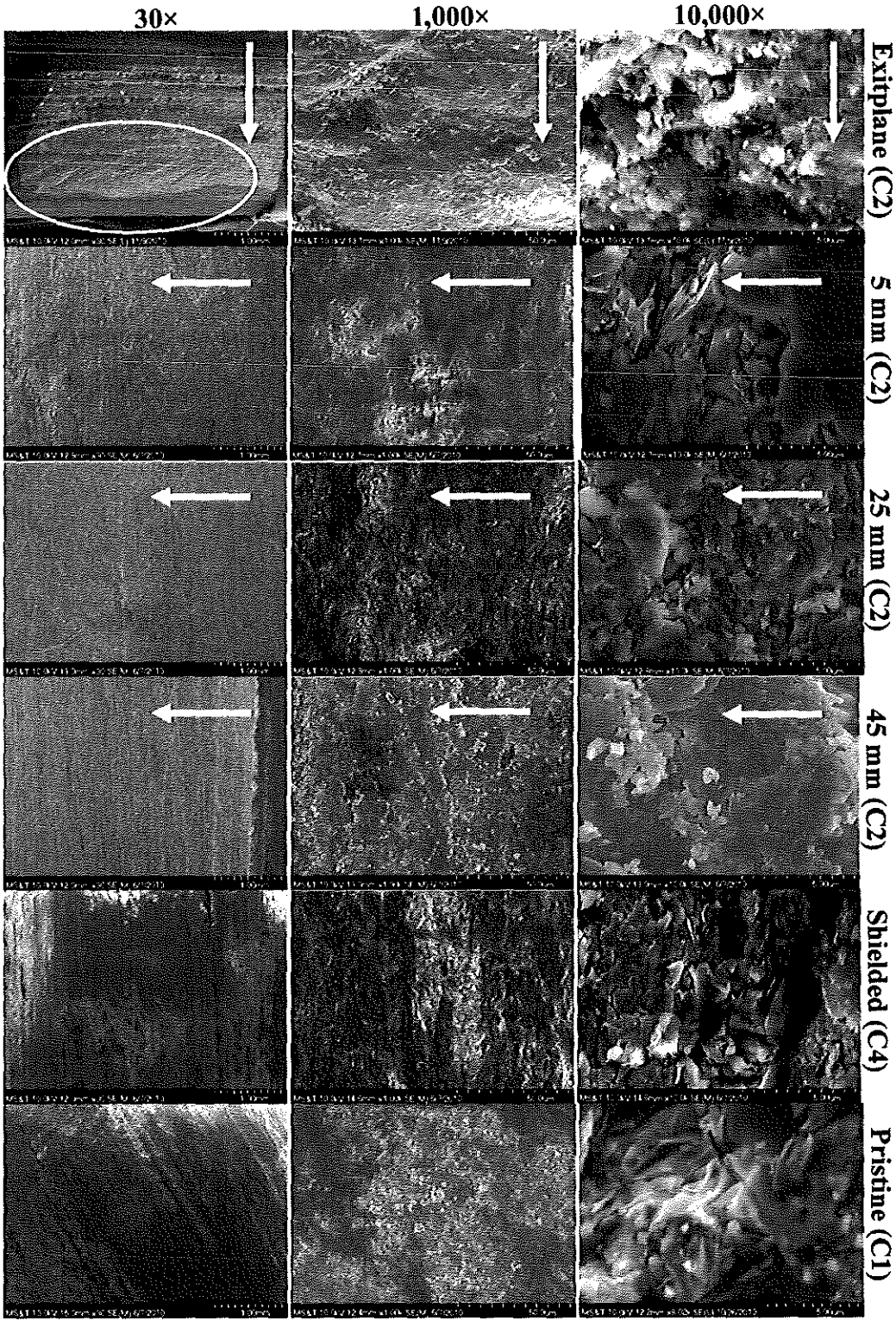

Figure 4.3. SEM Photographs of Samples C1, C2, and C4

Images at higher levels of magnification reinforce the trend that the exit plane has very different surface features than the 5, 25, and 45 mm locations, and the pristine and shielded samples. At 1000 times magnification the exit plane surface topography is highly irregular, and has much larger features (10's of μm across as opposed to 1 μm across) than all other frames at this level of magnification. Evidence of the macroscopic, angled grooves shown at 30 times magnification are still discernable at 1000 times. In the 1000 times magnification image of the exit plane, the crest of a hill can be seen in the top left and the valley at the bottom right corner. These types of features do not appear at the 5, 25, or 45 mm locations, or within the pristine or shielded images. At 10,000 times magnification, individual grains of BN become visible. These are the jagged structures that are visible in the 5 mm, 25 mm, 45 mm, pristine, and shielded images. Evidence of BN grains is not as apparent in the image of the exit plane. Instead the exit plane image shows a surface with white peaks and dark valleys.

Images of D samples at magnifications of 30, 100, 1,000, and 10,000 times are presented in Figure 4.4. At low magnification (30x, 100x) the image of the exit plane reveals grooves or striations. Similar to the C samples presented above, these structures are not purely in the axial direction, but are angled approximately 10° with respect to the axial direction and have a characteristic spacing of about 400 μm. The image near the anode shows large (> 1 mm) irregular surface features, while the shielded and pristine images reveal scratches due to the machining process. Unlike the C samples, there are no scratch marks or evidence of the machining process near the exit plane or anode. Both the exit plane and anode region of the D2 sample have more irregular visual surface features compared to the pristine and shielded samples.

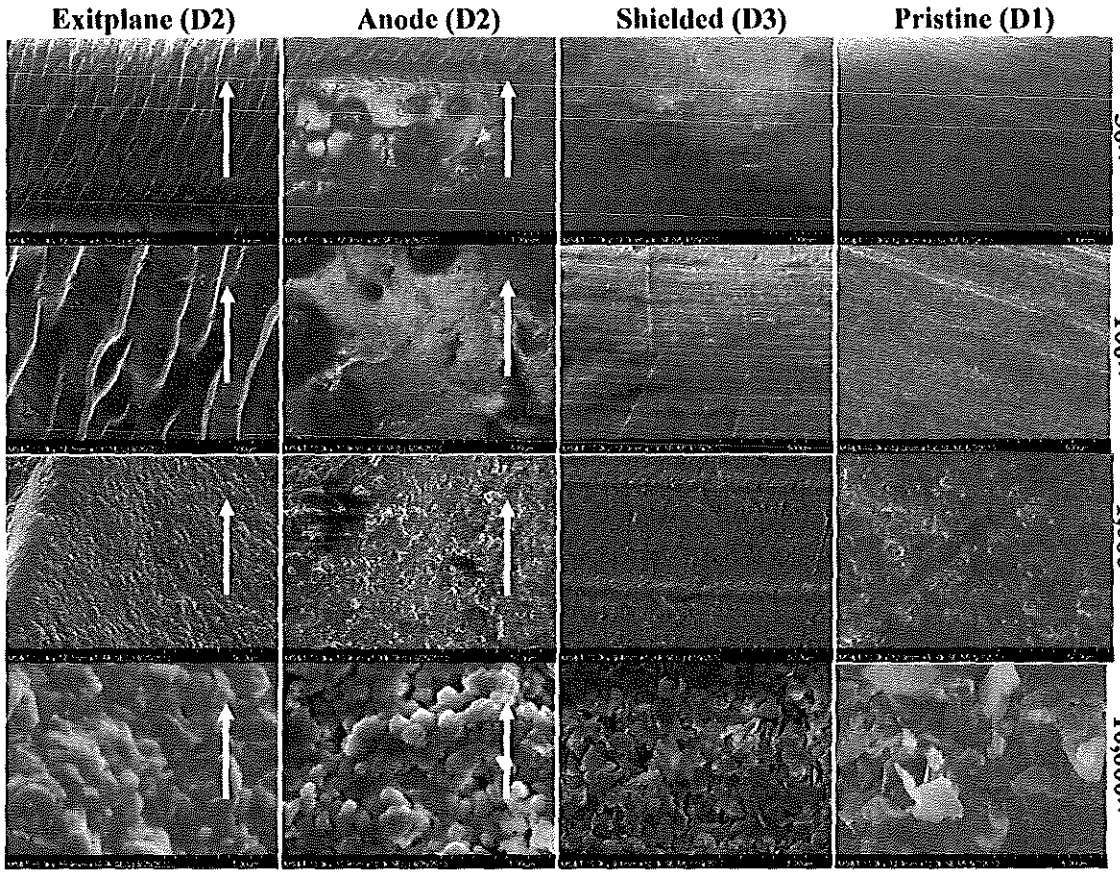

Figure 4.4. SEM Photographs of Samples D1, D2, and D3

Images at higher magnification also show differences between pristine and shielded samples, and the exit plane and near anode regions of the exposed sample. At 1,000 times magnification near the exit plane, the crest of a striation is shown on the left of the photograph. The surface morphology in this region of the thruster has changed to a more rounded morphology with an increased macroscopic roughness. Near the anode, at this level of magnification, the surface still appears irregular. Horizontal ridges due to the machining process are visible on the shielded sample, while a diagonal tool mark is visible on the pristine sample. These machining marks are not visible near the exit plane or anode of the exposed sample.

Images at 10,000 × magnification demonstrate a stark difference between the microstructure of exposed and shielded/pristine samples. Boron nitride grains, similar to those shown in Figure 4.3, are evident in the pristine and shielded samples. The shielded sample has grains that are smaller than those in the pristine sample. The characteristic size of a shielded sample grain is approximately 1 μm, while the pristine sample grains are roughly 2 μm. In both cases the grains appear jagged, with rough edges. Comparison of the pristine and shielded samples with the anode and exit plane regions shows that the microscopic structures are more rounded for the exposed sample. The image of the near anode region shows rounded, ball-like grains that have characteristic size of 1 μm. The grain structures near the exit plane are smoothed knobby protrusions, a magnification of the structures evident in the 1000 × image.

4.3. ENERGY DISPERSIVE X-RAY SPECTROSCOPY

Energy dispersive x-ray spectroscopy (EDS) analysis is performed at point locations on samples C1, C2, C4, D1, D2, and D3. The analysis is performed on C2 at 5 mm, 25 mm, and 45 mm from the exit plane. For the D2 sample, the analysis is performed near the exit plane and near the anode. The percentage by weight of each element found on the surface of the sample is tabulated in Table 4.3 and Table 4.4 for C and D samples, respectively. Also listed in Table 4.3 is the manufacturer quoted chemical composition of grade M26 BN,[26] this information is proprietary and not presented for grade HP.

EDS analysis of the pristine C sample shows good agreement with the 60% BN and 40% SiO_2 composition quoted by the manufacturer, differing by at most 9.5%. The shielded sample has 5% more nitrogen and 9% less silicon than the manufacturer quoted composition. Measurements at different locations along the exposed sample show that the fraction of boron and silicon are always less than the manufacturer quoted values, while the oxygen fraction is always larger. Further, the fraction of boron and nitrogen increase with proximity to the exit plane, while the fraction of silicon and oxygen decrease. Measurements also indicate the presence of carbon and metallic elements, and the

fraction of these species increases with proximity to the anode. Specifically, at 5 mm from the exit plane the percentage by weight of carbon is 5.9% and this fraction increases to almost 18% at 45 mm from the exit plane. At 45 mm from the exit plane, metallic elements (Al, Na, Mg, Cu, Fe) make up 3.3% of the surface by weight.

Table 4.3. EDS Analysis of the C1, C2, and C4 Samples (Percent by Weight)

Element	45mm	25mm	5mm	Shielded	Pristine	Manufacturer
B	10.5	18	20.5	25.7	23.2	26.5-28.7
N	21	36.6	42.2	39.7	29.5	32.8-35
O	30	23.9	22	20.4	24.4	21.3
Si	14.6	10.4	6.7	9.8	19.4	18.7
C	17.9	7.1	5.9	4.4	3.3	0
Na	0.5	0.4	0.5	0	0	0
Al	0.6	0.2	0	0	0.1	0
Mg	0.4	0.1	0	0	0	0
Cu	0.7	0	0	0	0	0
Fe	1.1	0	0	0	0	0
Cl	0.3	0	0	0	0	0

Analysis of the D samples is shown in Table 4.4 and shows similar trends to those found with the C samples. The base elemental components between the shielded and pristine samples tend to show good agreement, and agreement with the manufacturer specification that the sample is composed mainly of BN. Results indicate that the HP grade is composed of about 87% BN, with the remainder consisting of mainly oxygen and carbon. Similar to the C samples, results indicate that the fraction of BN increases with proximity to the exit plane, while silicon and oxygen decrease. In addition, the fraction of carbon increases with proximity to the anode. Unlike the C samples, less

metallic element deposition is present. The exception to this is sodium, which appears in decreasing concentrations with proximity to the exit plane of the thruster. An anomalous presence of low levels of fluorine is found in both the shielded and pristine specimens, this is potentially contamination during machining, or a product of the manufacture of original BN ceramic billets.

Table 4.4. EDS Analysis of the D1, D2, and D3 Samples (Percent of Elements By Weight)

Element	Anode	Exit	Shielded	Pristine
B	18.9	22	26.3	27.7
N	47.5	57.1	60.9	59.6
O	17.6	9.6	5.8	7.3
Si	0.6	0.2	0.5	0.2
C	10.6	7.8	2.6	2.9
Ca	0.6	0.4	3.6	0.5
Na	0.5	0.1	0	0
F	0	0	0.3	1

5. DISCUSSION

Using the results presented above, the following sections discuss the effects of 100's of hours of operation on the surface properties of a Hall thruster channel. Four discussion sections based on the main results from the study are presented. Differences in axial and azimuthal roughness are explained. Then the angled striations at the exit plane of both C and D samples are discussed. Next, changes in the surface at the microscopic level are examined. Finally, discussion of the surface chemical composition is presented.

5.1. ANISOTROPIC ROUGHNESS

Clear differences between axial and azimuthal roughness for the C and D samples are shown in Figure 4.1 and Table 4.2, respectively. Both shielded (C4) and exposed (C2) C sample results indicate that axial roughness is 2 times larger than azimuthal roughness. However, only the exposed D sample (D2) shows differences in axial and azimuthal roughness, the shielded sample (D3) does not. Neither pristine sample (C1 or D1, Table 4.1) show any roughness dependence on direction. The following discussion shows that some of these results can be explained by the machining process to fabricate the Hall thruster channel at beginning-of-life, while other results must be attributed to the wear process due to operation of the thruster.

At beginning-of-life, the C sample Hall thruster had axial roughness greater than azimuthal roughness due to the machining process of the thruster. After 100's of hours of operation, evidence of this anisotropic roughness is still present upstream of the exit plane, but absent at 5 mm from the exit plane. The C sample Hall thruster was manufactured by turning the original BN ceramic block on a lathe. This process causes the surface of the material to be covered in small ridges oriented in the azimuthal direction. These features can be seen in the low magnification SEM photos of Figure 4.3. Specifically, the photos at 25 and 45 mm, as well as the shielded specimen all show tool scratches due to the lathe process. During profilometry, if the scan is in the axial direction, the needle travels across these ridges yielding greater variance in the height of

the specimen surface, and thus determining greater roughness than a scan in the azimuthal direction. Careful inspection of the orientation of the scratches shown in the SEM photos of Figure 4.3 confirms that an axial profilometer scan travels across the ridges of the tool marks. As Figure 4.1 shows, at axial positions greater than 5 mm, axial roughness is always about 2 times greater than azimuthal roughness. This is a remnant of the beginning-of-life machining process. Closer to the exit plane, at 5 mm, axial and azimuthal roughness are comparable, suggesting evidence of the machining process has been removed. SEM photos at 5 mm (Figure 4.3) do not show the same tool marks as those farther upstream. Although roughness measurements are not available at the exit plane, SEM photos show deep azimuthal and angled grooves. Ion bombardment of the HET channel is known to cause greatest erosion at and near the exit plane, resulting in macroscopic (millimeter) changes to the channel profile [29, 39]. At the exit plane, erosion also appears to remove evidence of the anistropic roughness caused by the machining process.

Beginning-of-life machining cannot account for differences in axial and azimuthal roughness for the D sample Hall thruster. SEM photos of the shielded sample in Figure 4.4 reveal tool marks, but, as Table 4.2 shows, the shielded sample has only a 5% difference between axial and azimuthal scans. The exposed sample results show differences of 47% and 56% near the exit plane and anode, respectively. SEM photos in Figure 4.4 of the exit plane and anode regions show very different surface features from the shielded and pristine samples. Specifically, striations are present near the exit plane and an irregular surface is visible near the anode. These changes are due to the wear process of HET operation.

Pristine samples do not show a directional dependence on roughness. Due to the small dimensions of the pristine samples, they are not turned on a lathe to provide a sample surface similar to the sample surfaces on the thruster specimens. Instead, the test surface is faced off with a carbide mill tool to provide a smooth sample surface.

5.2. EXIT-PLANE ANGLED STRIATIONS

SEM results show regularly-spaced, angled grooves (striations) near the exit plane of both worn thruster samples, as seen in Figure 4.3 and Figure 4.4. The dominant wear mechanism near the exit plane in HETs is known to be ion bombardment sputtering erosion [6, 21, 24, 32]. This suggests that the angled grooves at the exit plane are due to impacting ions. The formation of striations is not unique to the Hall thruster channels investigated in this study. Several other examples of regularly-spaced wear patterns have been observed in laboratory HETs [6, 24]. These structures at the exit plane were initially observed in Soviet HET studies to be parallel to the ion flow and were proportional to the electron gyroradius [6]. Electron gyroradius can be calculated using Eqn. 2, where T_e is in units of eV and B is in units of Gauss [40]. Typical ranges of internal HET parameters are given in Table 5.1, [41, 42] along with the calculated electron gyroradius. From Figure 4.3 and Figure 4.4 above, the characteristic spacing of striations found in this study is approximately 400 μm for both worn HETs. This result falls within the 300-870 μm range of electron gyroradius in HETs.

$$r_e = \frac{2.38\sqrt{T_e}}{B} \tag{2}$$

Table 5.1. Typical Ranges of Internal HET Parameters

HET Parameter	Range
Te (eV)	10-30
B (G)	150-250
r_e (μm)	300-870

Striations at the exit planes of both thrusters exhibit a non-axial direction. Specifically, the C sample thruster shows grooved marks angled at approximately 30° to the axial direction, while the D sample thruster shows grooves angled at approximately

10°. Non-axial ion trajectories have been shown to be a result of magnetohydrodynamic (MHD) effects in a planar HET [43]. While ions are generally considered unmagnetized in HETs, the magnetic field may cause a deflection of the ion trajectory. However, a simple model using the Lorentz force shows MHD effects cannot cause the measured angles. The Lorentz force is given in Eqn. 3 and is iteratively solved to yield the trajectory of a singly-charged xenon ion accelerated through perpendicular electric and magnetic fields. The electric field is assumed to be a 300 V potential drop over 5 mm distance, while the magnetic field is 200 G and uniform throughout the acceleration region. With these assumed parameters, typical of an HET, an ion is only deflected ~0.4° by the time it exits the acceleration region. With a magnetic field of 2000 G (significantly larger than any HET), the ion has been deflected only 4°, still less than the measured angles. Curvature of ion trajectories by the HET magnetic field is not causing the angled striation profile.

$$\vec{F} = q\left(\vec{E} + \vec{v} \times \vec{B}\right) \tag{3}$$

Dependence of exit plane striation structures on the electron gyroradius clearly indicates that electrons play a significant role in the evolution of the wear and erosion of the channel wall, but currently no complete model has been able to explain this phenomenon [6]. However, recently, azimuthal electrostatic waves and electron stratification have been predicted via computational models, and observed experimentally [44, 45]. These results indicate that electrons do not drift uniformly in the Hall current, but instead bunch up, travelling in azimuthal waves around the thruster axis. Kinetic models by Pérez-Luna, *et.al.,* have shown this electron stratification in the azimuthal direction, which resembles the spokes of a wheel rotating around the thruster axis [44]. Electric fields resulting from electron stratification may preferentially focus plasma ions, resulting in the angled striations observed at the HET exit plane.

5.3. MICROSCOPIC GRAIN CHANGES

Evolution of the HET channel wall due to thruster operation occurs at both the macroscopic and microscopic level. Considering the SEM photographs (Figure 4.3 and Figure 4.4), macroscopic changes are those visible at low magnification (30x, 100x, characteristic length of 1 mm to 100's of μm), while microscopic changes are at higher magnification (smaller characteristic length, μm to nm). At the macroscopic level, beginning-of-life machining marks are removed and replaced by angled striations near the exit plane, and, for the D sample thruster, an irregular surface near the anode. The presence of macroscopic angled striations results in anisotropic roughness and these features are discussed in detail in the previous two sections. Evolution of the material surface at the microscopic level also occurs.

Differences in microscopic topography are observed between pristine, shielded, and exposed samples. As Figure 4.3 and Figure 4.4 show, all pristine and shielded samples have a jagged and fractured microstructure; these are the BN grains or crystallites. Locations upstream of the exit plane of the exposed C sample also show this same type of microstructure. However, regions near the exit plane of both exposed samples show a microscopic structure that is more rounded in comparison to the pristine and shielded samples. These changes are particularly apparent in the D specimen (Figure 4.4, 10,000×); both the exit plane and anode region of this sample have very different visual surface features compared to the pristine and shielded samples. The anode region of sample D has grains that appear as rounded balls, while the exit plane regions of both C and D samples have rounded knobby protrusions. The rounding off of these structures may be due to the propellant ions eroding the microstructure of the wall resulting in a more rounded wall microstructure. One other possibility for the formation of the rounded near wall microstructure may be the result of thermal effects on the ceramic material, but additional studies will be required to test this hypothesis.

5.4. CHEMICAL COMPOSITION COMPARISON

Energy dispersive x-ray spectroscopy results as a percentage by weight are shown in Table 4.3 and Table 4.4. To compare with results published by other researchers, these results are converted to atomic fraction using the molecular weight of each species. These results are presented in Table 5.2 and Table 5.3 for C and D samples, respectively.

Results in Table 5.2 show the atomic fraction of BN is one-to-one, while silicon dioxide (SiO_2) is one-to-two for the pristine sample. This one-to-one and one-to-two relationship is not maintained for the exposed sample, which suffered exposure to ion bombardment erosion. This result is contrary to that found by Garnier, *et.al.*, who subjected pristine M26 samples to ion bombardment erosion [29, 30]. Their results showed that BN and SiO_2 maintained a one-to-one and one-to-two relationship after exposure to sputter erosion. However, their experiments were conducted on pristine samples in a controlled environment and atomic fraction analysis did not indicate the presence of any atoms other than BN or SiO_2. Changes in HET channel atom fraction are different than those predicted by standard pristine sample sputtering erosion testing. Erosion studies conducted by bombarding pristine BN wafers may not provide a thorough representation of the erosion process at work within an HET. The presence of other atoms (carbon, metals) on the surface may be due to deposition of sputtered anode material or back sputtered beam dump material. Atomic sputtering rather than molecular sputtering as well as chemical erosion may be important.

Table 5.2. EDS Analysis of the C1, C2, and C4 Samples (Atom Fraction)

Element	Mass (g/mol)	45mm	25mm	5mm	Shielded	Pristine	Manufacturer
B	10.8	15	24.5	26.8	33	31.8	36.1
N	14	23	38.3	42.5	39.4	31.2	34.5
O	16	28.9	22	19.4	17.7	22.6	19.6
Si	28.1	8	5.4	3.4	4.9	10.3	9.8
C	12	23	8.7	6.9	5	4.0	0

Table 5.2 EDS Analysis of the C1, C2, and C4 Samples (Atom Fraction) (Continued)

Na	6.9	1	0.9	1	0	0	0
Al	27	0.3	0.1	0	0	0.1	0
Mg	24.3	0.2	0.1	0	0	0	0
Cu	63.6	0.2	0	0	0	0	0
Fe	55.8	0.3	0	0	0	0	0
Cl	35.5	0.1	0	0	0	0	0

Results in Table 5.2 indicate that the atom fraction of BN increases with proximity to the exit plane, while SiO_2 fraction decreases. The exit plane is the dominant region for sputtering erosion and previous work has shown that SiO_2 has higher sputter yield than BN [30]. Results in Table 5.2 support this conclusion because the surface atom fraction of silicon and oxygen atoms decreases, while boron and nitrogen increases with proximity to the exit plane. In other words, at regions closer to the exit plane, more SiO_2 has been removed by sputtering erosion, resulting in a higher atom fraction of BN. Previous work by Garnier, *et.al.,* disagrees with the results presented in Table 5.2 and also disagrees with sputter yield data. Specifically, their results showed that ion bombardment sputter erosion of a pristine M26 wafer caused an increase in SiO_2 fraction and decrease in BN, opposite to the trend shown in Table 5.2 and the trend expected based on the higher sputter yield of SiO_2 [30, 29].

The chemistry of the D samples, shown in Table 5.3, show similar variability to that of the C samples. Pristine and shielded specimens show good agreement on the initial composition of boron and nitrogen. The exposed portions of the specimen indicate larger amounts of oxygen, while the boron and nitrogen content decreases. The largest decrease in the boron and nitrogen is located closer to the anode, which is unexpected due to the fact that the majority of the sputtering erosion takes place near the exit plane of the thruster. This trend is also observed on the C samples. One possible explanation for the decreasing N and B content near the anode is that these atoms are being masked by the presence of other atoms that have been deposited onto the channel wall. The fraction of

atoms that mask the BN within the thruster channel decreases with proximity to the exit plane in agreement with the process of ions "cleaning" sputtered material from surfaces observed by Fife, *et al.* [12].

Table 5.3. EDS Analysis of the D1, D2, and D3 Samples (Atom Fraction)

Element	Anode	Exit	Shielded	Pristine
B	24.2	27.5	32.5	33.8
N	46.9	55.1	58.1	56
O	15.2	8.1	4.8	6
Si	0.3	0.1	0.2	0.1
C	12.2	8.8	2.9	3.2
Ca	0.2	0.1	1.2	0.2
Na	1	0.2	0	0
F	0	0	0.2	0.7

EDS analysis of both the C and D thrusters show carbon deposition, which may be a result of back-sputtered carbon from a graphite beam dump used during vacuum chamber testing; this carbon deposition initially has a fairly uniform concentration. The non-uniformity of carbon distribution may be a result of ions "cleaning" the BN surface at the exit plane where higher energy ion bombardment is present. The ion energy increases with proximity to the exit plane and as such the ions more efficiently "clean" the channel wall surface, thus resulting in decreasing carbon concentrations with proximity to the exit plane.

The EDS analysis of the Types C and D also demonstrate the metallization of the channel walls as observed by Raitses, *et al.*[46]. This is less apparent on the D samples where metallization consists solely of sodium, however the C samples show deposition of numerous metallic elements, with increasing quantities closer to the anode. The

deposition of metallic elements on the C samples include: aluminum, sodium, magnesium, copper, zinc, and iron, these are likely a result of anode material being sputtered onto the channel wall surfaces [46]. The decreasing concentration of these metallic elements with proximity to the exit plane is most likely to be the combined result of the ion "cleaning" of the channel walls, and the sputtered anode material being more densely distributed with proximity to the anode itself. This metallization of the channel wall, if given sufficient time, may result in a conductive layer, reducing the value of the BN wall material as an insulator, leading to enhanced electron losses along the wall and reducing the performance of the thruster.

6. CONCLUSIONS

Data gathered in this study demonstrate that surface properties of an HET channel after 100's of hours of operation differ from the surface properties of pristine BN ceramic and the beginning-of-life of the HET. Results from a high-power HET with grade M26 BN channel show a 73% increase in roughness near the exit plane, while upstream regions closer to the anode show an increase of only 12%. Results from a low-power HET with grade HP BN channel show exit plane roughness 5.4 times greater than a pristine sample. The microstructure of both thrusters exhibits more rounded surface features and crystallites. Additionally, there are changes to the composition of the channel wall after prolonged operation. The grade M26 BN channel shows losses of both silicon and oxygen in regions close to the exit plane where ion bombardment erosion is significant. Both HET channels show increased levels of carbon and metallic elements, with levels increasing with proximity to the anode.

Surface properties of HET channels are found to depend on axial position inside the channel. An HET channel generally becomes rougher near the exit plane. The C and D thrusters each have exit plane roughness that is 43% and 540% greater, respectively, than that near the anode. Atomic fraction of metals on the thruster wall increases from 0% near the exit plane to over 2% near the anode. Furthermore, atomic fraction of carbon increases from 8% near the exit plane to 23% near the anode. This material distribution may be the result of ions cleaning the channel walls with greater efficiency nearer the thruster exit where ion energies are greater and ion bombardment sputtering erosion is dominant. Both thrusters show grooved striated structures near the exit plane. These striations are a contributing factor in the increased measured roughness near the exit plane.

The roughness of HET channel walls is determined to be anisotropic. At beginning-of-life, anisotropy is due to the channel machining process, where turning the channel on a lathe causes axial roughness to be greater than azimuthal. Over time, ion bombardment erosion removes any evidence of machining. After 100's of hours of operation, striations angled 10° to 30° with respect to the axial direction develop. These macroscopic structures give rise to a new anisotropic roughness at the exit plane.

Evolution of the HET channel surface occurs on both the macroscopic and microscopic scale. Macroscopically, grooves and striations form near the exit plane of the thruster where ion bombardment erosion is dominant. Microscopically, individual ceramic grains are smoothed, resulting in more rounded and knobby near-wall structures. While individual grains become smoother, the roughness (i.e. vertical displacement) of the microscopic surface features tends to increase. While increased microscopic roughness is likely due to the preferential removal of high sputter yield silicon dioxide by ion bombardment, smoothing of individual grains has yet to be explained.

APPENDIX A.

SAMPLE ROUGHNESS CHARACTERIZATION PROTOCOL

The analysis of the surface roughness of the Boron Nitride Samples used in this thesis project is conducted using the Sloan Dektak IIA Surface Measuring System. The Dektak IIA Surface Measuring System is capable of measuring surface features having heights ranging from less than 100 Å to 655,000 Å. The Dektak IIA, as pictured in figure A1.1 utilizes a stylus tracing a path over the sample to measure the heights of the surface features.

The Dektak IIA consists of three primary components: the console, the scanning head, and the printer. The console contains the computer system which operates the entire apparatus, as well as the control keys, and the CRT monitor. The scanning head contains: the sample stage, a microscope and television camera, and the stylus assembly. The printer on the Dektak IIA used in this characterization procedure is not operational, and as such is not relevant to this protocol.

Figure A1.1. Sloan Dektak IIA Surface Measuring System. Dektak IIA components: Console: bottom right, Printer: top right, Scanning Head, left.

Setting up the profilimeter first requires the profilimeter to be turned on. The power switch for the profilimeter is located on the rear panel of the console in the upper left hand corner. See figure A1.2 for the location of the profilimeter power switch. Having turned on the profilimeter, the startup screen should be displayed on the profilimeter monitor. The screen should read: "SLOAN DEKTAK IIA REV. SO-C".

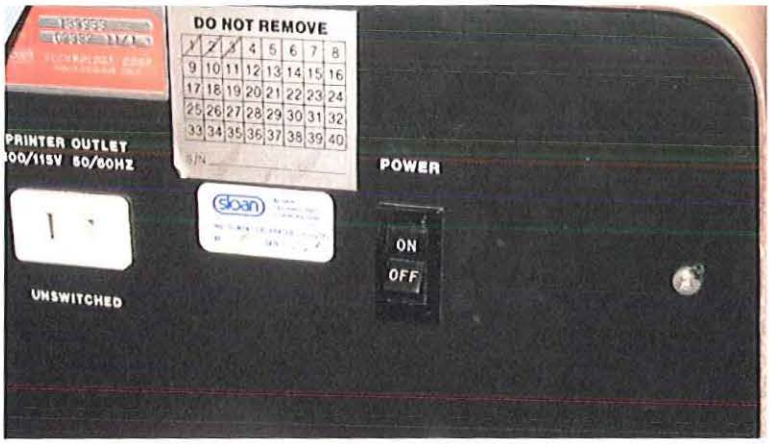

Figure A1.2. Power Switch Location. The power switch is located on the upper left hand side of the rear of the profilimeter console.

Having brought the profilimeter online, the sample should now be placed on the sample stage. The sample should be removed from its individually labeled sample bag, and placed on the stage underneath the stylus. Avoid touching the sample surface as the oils from human skin could potentially leave a residue capable of affecting the results of the characterization. Once the sample has been positioned on the stage it is recommended that the sample not be moved by hand again due to the risk of touching, and potentially damaging the stylus used to measure the surface profile. Once the sample has been positioned on the stage, it is recommended that to move the sample, a pencil or some other narrow object be used to push the sample to the desired position so as to alleviate the risk of touching, and damaging the stylus. An image of this procedure is available in figure A1.3.

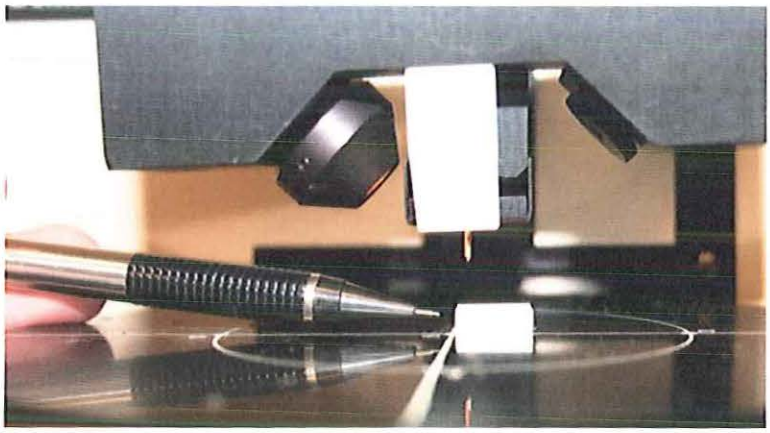

Figure A1.3. Positioning the Sample on the Stage

Leveling the sample on the sample stage of the scanning head is the final step in preparing the sample for characterization. On the console key board, as seen in figure A1.4, strike the *program* key, bringing the program menu onto the monitor. Figure A1.7 shows the profilometer program menu screen. Use the *direction* keys to select the *speed* category on the program menu. Change the speed setting to *HIGH* by, using the *direction* keys to highlight the *high* index, and then striking the *enter* key. On the console keyboard strike the *scan* key.

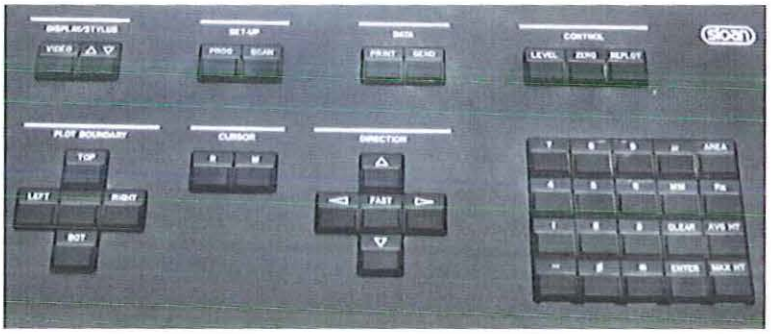

Figure A1.4. Console Keyboard

This will cause the scanning head to quickly scan the sample and produce an image of the screen of the surface profile. This surface profile will demonstrate the orientation of the sample surface as is demonstrated by the top image in figure A1.5.

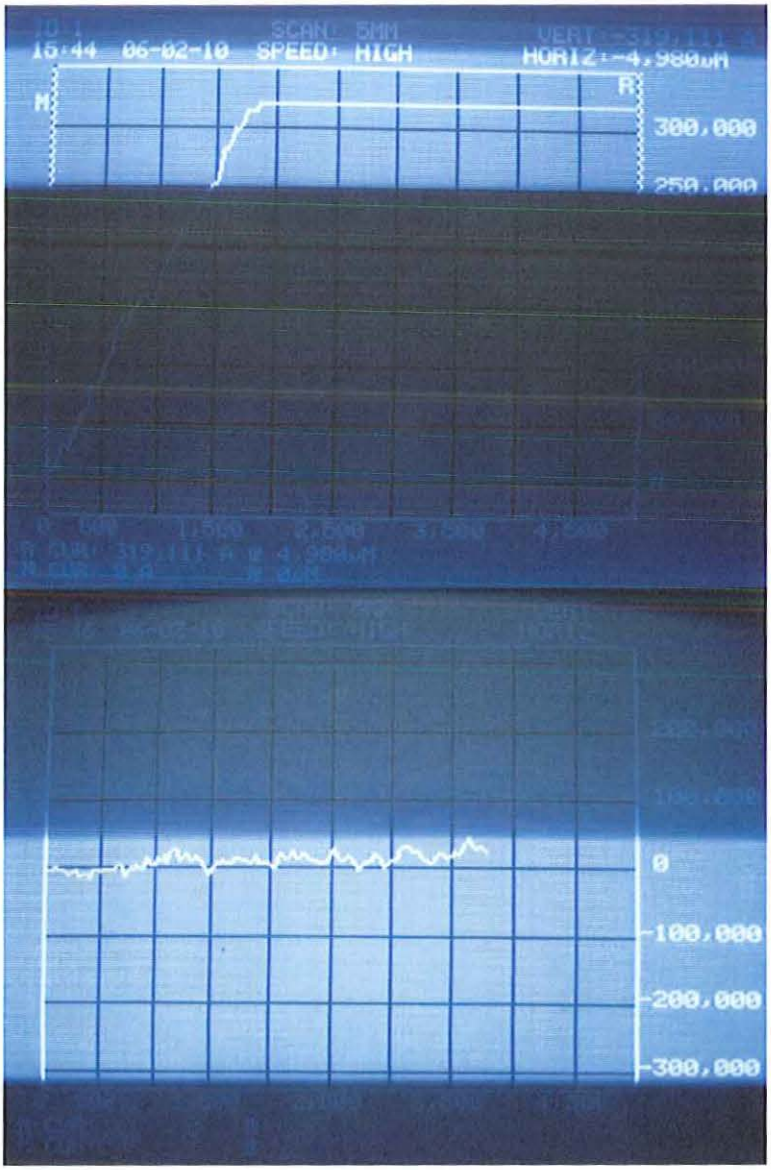

Figure A1.5. Surface Profiles. Surface profile before leveling, top; surface profile after leveling.

This surface is unleveled, and as such must be leveled. To level the surface, turn the leveling wheel under the sample stage. A photo of the leveling wheel is located in figure A1.6. To rotate the sample profile, and as such the sample stage in the clockwise direction, the leveling wheel must be turned in to the right, and to rotate the sample

profile in the counter-clockwise direction, the leveling wheel must be turned the leveling wheel to the left. When the line defining the surface profile lies approximately parallel to the zero axis of the grid on the console monitor the sample is considered level, at this point the surface profiling may begin.

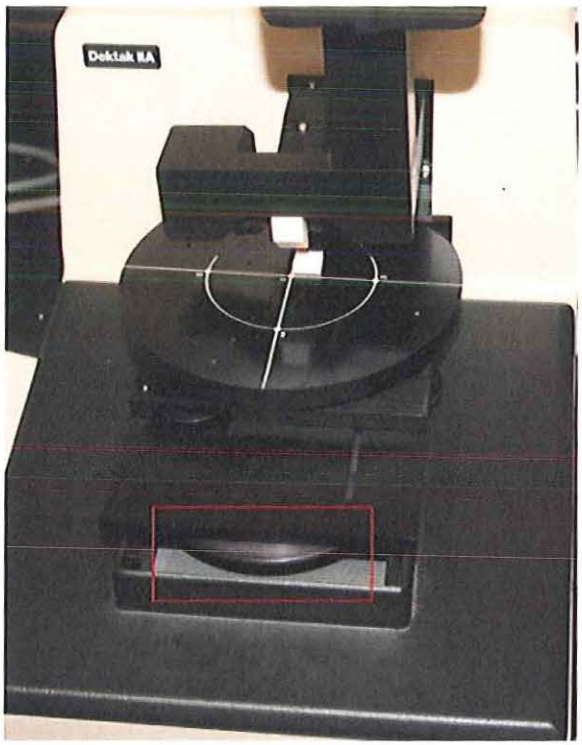

Figure A1.6. Leveling Wheel. Note the location of the leveling wheel on the Scanning Head has been outlined in red.

Figure A1.7. Menu Screen of the DEKTAK IIA Profilometer

To profile the sample surface, strike the *program* key to access the menu. Use the cursor keys on the console to change the speed setting to *low*. The sample is now ready to be profiled for surface roughness. The profiling procedure is to conduct three scans at three locations along the sample; the three locations should be 2 to 4 millimeters apart. The sample must then be rotated 90 degrees and then the sample should be profiled as described earlier: three scans per location at three locations 2 to 4 millimeters apart. The scanning pattern for a sample is shown in fig A1.8.

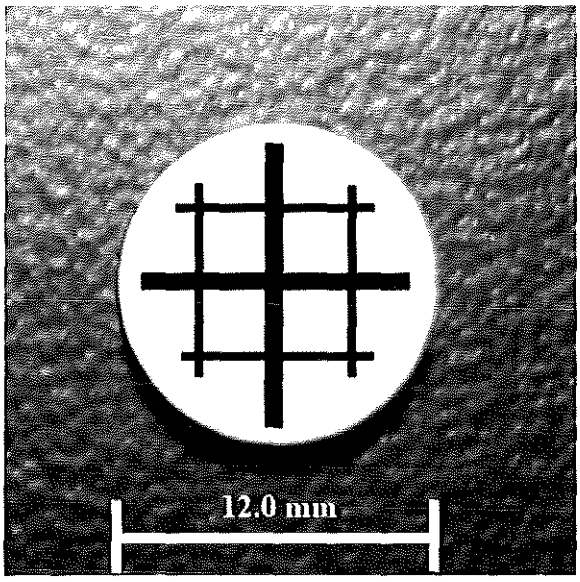

Figure A1.8. Scanning Pattern

Upon completion of the scan the profilometer will replot the data from the scan on the console screen. To normalize the data, the data must be leveled and zeroed to ensure that all data recorded with respect to a common reference point. The first normalization step is to level the data. To level the data, strike the *level* key on the console keyboard. The data will then be replotted on the screen and leveled with respect to the average point height. Once the leveled data is replotted to the screen, the data should be zeroed. To zero the data, strike the *zero* key on the console keyboard. The data will again be replotted, this time zeroed with respect to an average height.

The surface data may now be determined and recorded. The profilometer is capable of producing three different surface characteristics: roughness, average height, and max height. To determine the roughness, strike the *Ra* key on the console keyboard. When the *Ra* key is struck the *RA* = will appear on the lower right hand corner of the console screen, this indicates that the profilometer is computing the surface roughness. Once the console has completed computing the surface roughness, the value of the roughness in angstroms will appear next to the *RA* =. The average surface height and the maximum

surface height may then be determined similarly by striking the *AVG HT*, and *MAX HT* keys respectively. The data cannot be saved by the profilometer in its current configuration, and at present cannot be exported to another device; as such, the recommended data recording procedure is to enter the data into a spreadsheet program such as Microsoft Excel where it may be saved for further analysis.

APPENDIX B.

COMPUTER PROGRAM SOURCE CODES

This program, *electron_gyroradius.m* is a MATLAB script used to determine the electron gyroradius for conditions similar to those found in a typical 200 Watt Hall-thruster as discussed in Chapter 5.1.

```
%Program Name: electron_gyroradius.m
%==========================================================================
%   Program Author:                 Date Written:
%   ===============         ============================
%    David Zidar           Friday, 12 November 2010
%==========================================================================
%Description of Program:
%   This program calculates the trajectory of an Xe+1 ion accelerated by
%   electric and magnetic fields.
%==========================================================================
%Record of Revisions.
%   Date of Revision:                  Description of Revision
% ========================   ============================================
% Friday, 12 November 2010   Original Code
%==========================================================================
%Begin executable code.
%**************************************************************************
%Clear the Command Space, Current Directory, all Open Figures, and Close
%all Open Figures.
clear all;
clc;
clf;
close all;
%**************************************************************************
%Notify the user that the program is running.
fprintf('Running Program: electron_gyroradius.m\n');
%**************************************************************************
%Assign Variables and Allocate Memory.
eT = 5; %Electron Temperature [eV] (REF 4)
D = 0.0291; %Distance Between Striations [cm]
%B = 1400;
B = 200; %Approximate Magnetic field for a 200 Watt HET [Gauss] (Ref 2)
%B = 92.8;
%**************************************************************************
%Compute the electron radius for the BHT-200 HET.
    %Calculate the Electron Gyroradius.
    re = 2.38*sqrt(eT)/B; % (Ref 3)
    %Calculate the required electron temperature required to generate the
    %electron gyroradius equal to the striation spacing.
    T = (D*B/2.38)^2;
%**************************************************************************
%Print out the data to the screen.
fprintf('B = %5.3f [G]\n',B);
fprintf('T = %5.3f [eV]\n',eT);
fprintf('The Electron GyroRadius is: %5.8f [micron]\n',re*10000);
fprintf('The Electron Temperature required for spacing\n to match electron
gyroradius is: %10.10f [eV].\n',T);
%**************************************************************************
%Notify the user that the program is complete.
fprintf('Program Complete\n...');
%**************************************************************************
%References:
%   [1] Ekholm, J. & Hargus, W. (2005)ExB Measurement of a 200 W Xenon Hall
%       Thruster, AIAA-2005-4405,pp. 4,6-7.
%   [2] Micci, M. M. & Ketsdever, A. D. (2000) Micropropulsion for small
```

```
%       spacecraft, AIAA, Reston, VA, pp. ~258.
%   [3] Huba, J. D. (2007) NRL Plasma Formulary, Naval Research Laboratory,
%       Washington, DC, pp. 28.
%   [4] Nakles, Brieda, et. al. (2007) Experimental and Numerical
%       Examination of the BHT-200 Hall Thruster Plume, AIAA 2007-5305
%*************************************************************************
%End of Program Code.
%*************************************************************************
```

This program, *TimeMarchingModel.m* was used to determine the trajectory of a single Xe^{+1} ion in conditions similar to a 200 Watt Hall-thruster as discussed in Chapter 5.1.

```
%Program name: TimeMarchingModel.m
%=========================================================================
%   Program Author:                 Date Written:
%   ===============         ============================
%    David Zidar              Saturday, 23 October 2010
%=========================================================================
%Description of Program:
%   This program calculates the trajectory of an Xe+1 ion accelerated by
%   electric and magnetic fields.
%=========================================================================
%Record of Revisions.
%   Date of Revision:                   Description of Revision:
% ========================   ========================================
% Saturday, 23 October 2010   Original Code
%=========================================================================
%Begin executable code.
%*************************************************************************
%Clear the command space, the current directory, all open figures and close
%all open panes.
clear all;
clc;
clf;
close all;
%*************************************************************************
%Notify the user that the program is running.
fprintf('Running Program: TimeMarchingModel.m...\n');
%*************************************************************************
%Assign variables.
E_max = 200; %Max voltage [V]
E_0 = 0;    %Min voltage [V]
q = 1.6*(10^-19);   %Elementary Charge [C]
mXeplus1 = 2.19341*(10^-25);    %Mass of a Xe+1 atom.
d = 0.1;  %Length of the acceleration region [m]
B = 0.05;   %Magnetic field strength [T]
kB = 1.3806503*(10^-23);    %Boltzman Constant (m^2 kg)/(s^2 K)
T = 500;    %Temperature of Xe+1 entering the thruster.
dt = 1e-9;   %Timestep [s]
z(1,1) = 0;   %Initial location in the z-direction [m]
r(1,1) = 0;   %Initial location in the r-direction [m]
ii = 2;
%*************************************************************************
%Solve for the initial velocity in the z and radial directions.
V_r(1,1) = 0;
V_z(1,1) = sqrt(kB*T/(pi*mXeplus1));
%*************************************************************************
```

```
%Time march forward until the particle has passed through the acceleration
%region.
while z(ii-1,1) < d
z(ii,1) = z(ii-1,1) + V_z(ii-1,1)*dt + 0.5*dt*dt*((E_max-E_0)/d)*q/mXeplus1;
r(ii,1) = r(ii-1,1) + V_r(ii-1,1)*dt + 0.5*dt*dt*q*V_z(ii-1,1)*B/mXeplus1;
V_z(ii,1) = (z(ii,1)-z(ii-1,1))/dt;
V_r(ii,1) = (r(ii,1)-r(ii-1,1))/dt;
ii = ii + 1;
end
%*************************************************************************
%Calculate the energy of the Xe+1 ion.
E = 0.5*mXeplus1*(V_z(ii-1)^2 + V_r(ii-1)^2)/q;
V = V_z + V_r;
%*************************************************************************
%Print out relevant data to the screen.
fprintf('\nGiven Xe+1 and: \n');
fprintf('Input Voltage = %4.2f V\n',E_max);
fprintf('B = %4.2f T\n',B);
fprintf('Acceleration distance = %5.7f m\n',d);
fprintf('Initial Temperature = %4.2f K\n',T);
fprintf('THETA = %3.7f degrees \n',atand(V_r(ii-1)/V_z(ii-1,1)));
fprintf('THe Xe+1 ion has energy E = %5.4f eV\n',E);
fprintf('Duration of acceleration %4.8f microseconds\n',(ii*dt)*1e6);
fprintf('Terminating exit velocities, Vr = %9.2f m/s, Vz = %9.2f m/s\n',V_r(ii-
1),V_z(ii-1));
%*************************************************************************
%Plot out the relevant data.
figure(1);
plot(z,V_z,'b--');
hold on;
plot(z,V_r,'r-.');
xlabel('Distance [m]');
ylabel('Velocity [m/s]');
title('Particle Velocities');
legend('Vz','Vr');
figure(2);
plot(z,r);
hold on;
xlabel('z');
ylabel('r');
title('Particle Trajectory')
%*************************************************************************
%Notify the user that the program is complete.
fprintf('\nProgram Complete...\n');
%=========================================================================
%End of Program Code
%=========================================================================
```

BIBLIOGRAPHY

[1] Seikel, G. R. and Reshotko, E., "Hall Current Ion Accelerator," *Bulletin of the American Physical Society*, 1962, Vol. 7, No. 6, pp. 414.

[2] Hess, R. V., "Fundamentals of Plasma Interaction With Electric and Magnetic Fields," *Plasma Physics and Magnetohydrodynamics in Space Exploration*, NASA SP-25, December 1962, pp. 20-23.

[3] Seikel, G. R., "Generation of Thrust-Electromagnetic Thrusters," *Electric Propulsion for Spacecraft*, NASA SP-22, December 1962, pp. 21.

[4] Cann, G. L. and Marlotte, G. L., "Hall Current Plasma Accelerator," *AIAA Journal*, Vol. 2, No. 7., 1964, pp. 1234-1241.

[5] Choueiri, E. Y., "Fundamental Difference Between Two Hall Thruster Variants," *Physics of Plasmas*, 2001, Vol. 8, No. 11., pp. 5025.

[6] Morozov, I. A., "The Conceptual Development of Stationary Plasma Thrusters," *Plasma Physics Reports*, [Translated from Russian. Originally published in: *Fizika Plazmy*, Vol. 29, No. 3, pp. 261-276.] Vol. 29, No. 3, 2003, pp. 235-250.

[7] Foing, B. H., Racca, G. D., Evrard, E., Stagnaro, L., Almeida, M., Koschny, D., Frew, D., Zender, J., Heather, J., Grande, M., Huovelin, J., Keller, H. U., Nathues, A., Josset, J. L., Malkki, A., Schmidt, W., Noci, G., Birkl, R., Iess, L., Sodnik, Z., McManamon, P., "SMART-1Mission to the Moon: Status, first results, and goals," *Advances in Space Research*, Vol. 37, No. 1., 2006, pp. 6-13.

[8] Racca, G. D., Marini, A., Stagnaro, L., van Dooren, J., di Napoli, L., Foing, B. H., Lumb, R., Volp, J., Brinkmann, J., Grünagle, R., Estublier, D., Tremolizzo, E., McKay, M., Camino, O., Schoemaekers, J., Hechler, M., Khan, M., Rathsman, P., Andersson, G., Anflo, K., Bergee, S., Bodin, P., Edfors, A., Hussain, A., Kugelberg, J., Larsson, N., Ljung, B., Meijer, L., Mörtsell, A., Nordebäck, T., Persson, S., Sjöberg, F., "SMART-1 mission description and development status," *Planetary and Space Science*, Vol. 50, No. 14-15, 2002, pp. 1323-1337.

[9] Flemming, E. S., Lafleur, J. M., and Saleh, J. H., "Response Surface Equations for Expendable Launch Vehicle Capability," *AIAA SPACE 2009 Conference and Exposition*, AIAA, 2009.

[10] Jacobson, D. T., Mazella, D. H., Hofer, R. R., and Peterson, P. Y., "NASA's 2004 Hall Thruster Program," *40th Annual AIAA/ASME/SAE/ASEE Joint Propulsion Conference and Exhibit*, AIAA, 2004.

[11] Jankovsky, R. S., Jacobson, D. T., Rawlin, V. K., Mazella, D. H., Hofer, R. R., and Peterson, P. Y., "NASA's Hall Thruster Program," *37th Annual AIAA/ASME/SAE/ASEE Joint Propulsion Conference and Exhibit*, AIAA, 2001.

[12] Fife, J. M., Gibbons, M. R., Hargus, W. A., VanGilder, D. B., and Kirtley, D. B., "3-D Computation of Surface Sputtering and Redeposition Due to Hall Thruster Plumes," *International Electric Propulsion Conference*, IEPC, 2003.

[13] Hofer, R. R., Mikellides, I. G., Katz, I., and Goebel, D. M., "Wall Sheath and Electron Mobility Modeling in Hybrid-PIC Hall Thruster Simulations," *43rd AIAA/ASME/SAE/ASEE Joint Propulsion Conference and Exhibit*, AIAA, 2007.

[14] Ivanov, A. A., Ivanov Jr., A. A. and Bacal, M., "Effect of plasma-wall recombination on the conductivity of Hall thrusters," *Plasma Physics and Controlled Fusion*, Vol. 44, No. 7, 2002, pp. 1463-1470

[15] Sommier, E., Allis, M. K., Gascon, N., and Cappelli, M. A., " Wall Erosion in 2D Hall Thruster Simulations," *42nd AIAA/ASME/SAE/ASEE Joint Propulsion Conference and Exhibit*, AIAA, 2006.

[16] Sullivan, K., Fox, J., Martinez-Sanchez, and M., Batischev, O., "Kinetic Study of Wall Effect in SPT Hall Thrusters," *40th AIAA/ASME/SAE/ASEE Joint Propulsion Conference and Exhibit*, AIAA, 2004.

[17] Locke, S., Shumlak, U. and Fife, J. M., "Effect of a Channel Wall Discontinuity in an SPT-Type Hall Thruster," *37th AIAA/ASME/SAE/ASEE Joint Propulsion Conference*, AIAA, 2001.

[18] Raitses, Y., Staack, D., Keidar, M., and Fisch, N. J., "Electron-wall interaction in Hall thrusters," *Physics of Plasmas*, Vol. 12. No. 5, 2005, pp. 057104-1 – 057104-9.

[19] Dunaevsky, A., Raitses, Y. and Fisch, N. J., "Secondary electron emissions from dielectric materials of a Hall thruster with segmented electrodes," *Physics of Plasmas*, Vol. 10, No. 6, 2003, pp. 2574-2577.

[20] Raitses, Y., Smirnov, A., Staack, D.,and Fisch, N. J., "Measurements of secondary electron emission effects in the Hall thruster discharge," *Physics of Plasmas*, Vol. 13, No. 1, 2006, pp. 014502-014502-4.

[21] Peterson, P. Y., Jacobson, D. T., Manzella, D. H., and John, J. W., "The Performance and Wear Characterization of a High-Power High-Isp NASA Hall Thruster," *41st AIAA /ASME/SAE/ASEE Joint Propulsion Conference and Exhibit*, AIAA, 2005.

[22] Mason, L. S., Jankovsky, R. S. and Manzella, D. H., "1000 Hours of Testing on a 10 Kilowatt Hall Effect Thruster," *37th AIAA /ASME/SAE/ASEE Joint Propulsion Conference and Exhibit*, AIAA, 2001.

[23] Gorschkov, O., Shagayda, A. and Muravlev, V., "The Experience of Hall Thruster Research and Development," *57th International Astronautical Congress*, IAC, 2006. pp. 1-8.

[24] de Grys, K., Mathers, A., Welander, B., and Khayms, V., "Demonstration of 10,400 Hours of Operation on a 4.5 kW Qualification Model Hall Thruster," *46th AIAA/ASME/SAE/ASEE Joint Propulsion Conference &Exhibit*, AIAA, 2010.

[25] Sydorenko, D., Smolyakov, A., Kaganovich, I., Raitses, Y., " Kinetic Simulation of Effects of a Secondary Electron Emission on Electron Temperature in Hall Thrusters," *The 29th Annual International Electric Propulsion Conference*, IEPC, 2005.

[26] Zhurin, V. V., Kaufman, H. R., and Robinson, R. S., "Physics of closed drift thrusters," *Plasma Sources Science and Technology*, Vol. 8, No. 1, 1999, pp. R1-R20.

[27] Gascon, N., Dudeck, M., and Barral, S., "Wall material effects in stationary plasma thrusters. I. Parametric studies of an SPT-100," *Physics of Plasmas*, Vol. 10, No. 10, 2003, pp. 4123-4136.

[28] Yong, Y. C., Thong, J. T. L., and Phang, J. C. H., "Determination of secondary electron yield from insulators due to a low-kV electron beam," *Journal of Applied Physics*, Vol. 84, No. 8, 1998, pp. 4543-4548.

[29] Garnier, Y., Viel, V., Roussel, J. F., and Bernard, J., " Low-energy xenon ion sputtering of ceramics investigated for stationary plasma thrusters," *Journal of Vacuum Science and Technology*, Vol. 17, No. 6, 1999, pp. 3246-3254.

[30] Garnier, Y., Viel, V., Roussel, J. F., Pagnon, D., Mange, L., and Touzeau, M., "Investigation of Xenon Ion Sputtering of One Ceramic Material Used in SPT Discharge Chamber," *26th International Electric Propulsion Conference*, IEPC, 1999, pp. 512-517.

[31] Tondu, Th., Viel-Inguimbert, V., Roussel, J. F., and D'Escrivan, S., "Hall Effect Thrusters ceramics sputtering yield determination by Monte Carlo simulations," *44th AIAA/ASME/SAE/ASEE Joint Propulsion and Exhibit* , AIAA, 2008.

[32] Peterson, P. Y. and Manzella, D. H., "Investigation of the Erosion Characteristics of a Laboratory Hall Thruster," *39th AIAA/ASME/SAE/ASEE Joint Propulsion Conference and Exhibit*, AIAA, 2003.

[33] St. Gobain Advanced Ceramics, "Combat® Solid Boron Nitride Grade A," [Online resource], URL: http://www.bn.saint-gobain.com/uploadedFiles/SGbn/Documents/Solids/Solid-Combat-BN-GradeA.pdf. [Cited: September 9, 2010].

[34] St. Gobain Advanced Ceramics, "Combat® Solid Boron Nitride Composite Grade HP," [Online resource], URL: http://www.bn.saint-gobain.com/uploadedFiles/SGbn/Documents/Solids/Solid-Combat-BN-GradeHP.pdf. , [Cited: September 9, 2010].

[35] St. Gobain Advanced Ceramics, "Combat® Solid Boron Nitride Composite Grades M and M26," [Online resource], URL: http://www.bn.saint-gobain.com/uploadedFiles/SGbn/Documents/Solids/Solid-Combat-GradesM-M26.pdf., [Cited: September 9, 2010].

[36] DeGarmo, E., P., Black, J. T., and Kohser, R. A., *Materials and Processes in Manufacturing 8th edition*, Prentice Hall, Upper Saddle River, NJ, 1997, pp. 288-295.

[37] Sloan Technology Corporation, *Dektak IIA Manual*, Sloan Technology Corporation, Santa Barbara, CA, 1984, pp. i.

[38] Goldstein, J. I., Newbury, D. E., Echlin, P., Joy, D. C., Romig, Jr., A. D., Lyman, C. E., Fiori, C., Lifshin, E., *Scanning Electron Microscopy and X-ray Microanalysis. 2nd edition*, Plenum Press, New York. 1992, pp. 21-25,292-311.

[39] Pagnon, D., Lasgorceix, P., and Touzeau, M., "Control of the Ceramic Erosion by Optical Emission Spectroscopy: Results of PPS1350-G Measurements," *4th International Spacecraft Propulsion Conference*, ISPC, 2004.

[40] Huba, J. D., *NRL Plasma Formulary*, Naval Research Laboratory, Washington, DC, 2007, pp. 28.

[41] Haas, J. M. and Gallimore, A. D., "Considerations on the Role of the Hall Current," *Transactions on Plasma Science*, Vol. 30, No. 2, pp. 687-697.

[42] Smirnov, A., Raitses, Y. and Fisch, N. J., "Parametric investigation of miniaturized cylindrical and annular," *JOURNAL OF APPLIED PHYSICS*, Vol. 92, No. 10, 2002, pp. 5673-5679.

[43] Rovey, Joshua L., Giacomi, M. P., Stubbers, R. A., and Jurczyk, B. E., "Plume Profiles of a Planar Crossed Field-Thruster with Hall Current Injection," *Journal of Propulsion and Power*, Vol. 25, No. 3, 2009, pp. 737-745.

[44] Perez-Luna, J., Hagelaar, G. J. M., Garrigues, L., Dubuit, N., and Boeuf, J. P., "Influence of azimuthal instabilities on electron motion in a Hall Effect Thruster," *International Electric Propulsion Conference,* IEPC, 2007.

[45] Kaganovich, I. D., "Modeling of collisionless and kinetic effects in thruster plasmas," *27th International Electric Propulsion Conference*, IEPC, 2005.

[46] Raitses, Y., Dorf, L. A., Litvak, A. A., and Fisch, N. J., "Plume reduction in segmented electrode Hall thruster," *Journal of Applied Physics*, Vol. 88, No. 3, 2000, pp. 1263-1270.

VITA

David George Zidar was born on November 15, 1986 in Youngstown, Ohio. In 2008, David worked as a student researcher in the National Science Foundation's Research Experience for Undergraduates Program in Complex Fluids at Washington University in St. Louis, Missouri. In May 2009 he received his Bachelor of Science degree in Aerospace Engineering from Parks College of Engineering, Aviation and Technology at Saint Louis University in St. Louis, Missouri. While at Saint Louis University, David was involved in multiple research projects resulting in two AIAA student conference papers, an ASEE conference paper, and winning first and second place respectively in the Saint Louis University and Missouri-Illinois Regional Idea to Product Competition.

He is currently pursuing a Master of Science degree in Aerospace Engineering at Missouri University of Science and Technology in Rolla, Missouri. Following his graduation from Missouri University of Science and Technology in May 2011, David will begin working as a Product Review Engineer for the Boeing Company Commercial Aircraft Division in Everett, Washington.